

ARE THERE SEXTUPLET AND OCTUPLET IMAGE SYSTEMS?

N. Wyn Evans¹ and Hans J. Witt²

¹ *Theoretical Physics, 1 Keble Rd, Oxford, OX1 3NP*

² *University of Manchester, Jodrell Bank Observatory, Macclesfield, Cheshire, SK11 9DL*

30 October 2018

ABSTRACT

We study gravitational lensing by the family of scale-free galaxies with flat rotation curves. The models are defined by a shape function, which prescribes the radius of the isophote as a function of position angle from the major axis. The critical curves are analytic, while the caustic network is reducible to a simple quadrature. The cusps are always located at the turning points of the shape function. We show that the models with exactly elliptic isophotes never admit butterfly or swallowtail cusps and so have at most 4 (or 5) images. Higher order imaging is brought about by deviations of the isophotes from pure ellipses – such as pointedness caused by embedded disks or boxiness caused by recent merging. The criteria for the onset of sextuple and octuple imaging can be calculated analytically in terms of the ellipticity ϵ and the fourth-order Fourier coefficients (a_4 and b_4) used by observers to parametrise the isophote shapes. The 6 or 8 images are arranged roughly in a circle, which appears as an incomplete Einstein ring if inadequately resolved. Using data on the shapes of elliptical galaxies and merger remnants, we estimate that $\sim 1\%$ of all multiply imaged quasars may be sextuplet systems or higher. Forthcoming satellites like the Global Astrometric Interferometer for Astrophysics (GAIA) will provide datasets of ~ 4000 multiply imaged systems, and so ~ 40 will show sextuple imaging or higher.

Key words: gravitational lensing – galaxies: structure – galaxies: elliptical – dark matter

1 INTRODUCTION

Almost all the known sixty or so gravitational lens systems are 2 or 4 image configurations (see Pospieszalka et al. 1999 for details of the gravitational lensing database which maintains a list of candidates). There are two systems in which the presence of a weak, central image has been claimed, namely APM08279+5255 (Ibata et al. 1999) and MG1131+0456 (Chen & Hewitt 1993), but these detections are controversial. There are only two lens systems which are definitely established to have more than 4 images of a single source. The first is CL0024+1654 which comprises 8 images of a single blue galaxy lensed by a foreground cluster of galaxies (Colley, Tyson & Turner 1996; Tyson, Kochanski & Dell’Antonio 1998). The second is B1359+154, which consists of 6 images of a single radio source (Rusin et al 2001). Here, the lens is believed to be a compact group of galaxies.

For non-singular lenses, it is well-known that the total number of images is odd and that the number of even parity images exceeds the number of odd parity images by one (e.g., Burke 1981; Schneider, Ehlers & Falco 1992, chap. 5). When the source lies within the central or tangential caustic, such lenses typically give rise to 5 images. Four of these lie

roughly on an Einstein ring, while the fifth is highly demagnified and located near the centre of the lensing galaxy. For cusped lenses, the convergence (or surface density in units of the critical density) κ behaves like

$$\lim_{r \rightarrow 0} \kappa(r) = O(r^{-\gamma}), \quad (1)$$

and so diverges at the galaxy centre. Evans & Wilkinson (1998) showed that there are 4 images if the central cusp is stronger than isothermal ($\gamma > 1$), and 5 images if the cusp is weaker than isothermal ($\gamma < 1$), again assuming the source lies within the central caustic. Hence, the observed abundance of 4 image systems may be caused either by strong cusps (in which case there are only 4 images) or by small core radii (in which case the fifth image is so demagnified as to be invisible against the much brighter lensing galaxy).

The purpose of this paper is to ask whether sextuplet or octuplet images may exist? If so, what properties of the lensing galaxy cause such higher order imaging? Note that in this paper, by a slight abuse of terminology, we use sextuple imaging to refer to systems with 6 or 7 images; a central seventh image may exist if the galaxy is soft-centered but will in general not be discernible. Similarly, octuple imaging

arXiv:astro-ph/0108374v1 23 Aug 2001

may refer to 8 or 9 images. Systematic programs like the Cosmic Lens All-Sky Survey or CLASS (e.g., Myers et al 1995, Myers 1999) are now providing a much larger dataset of multiply-imaged quasars than the earlier serendipitous discoveries. The future holds out even brighter prospects, as the Next Generation Space Telescope (NGST) and the Global Astrometric Interferometer for Astrophysics (GAIA) will discover many thousands of such systems (e.g., Barkana & Loeb 2000; de Boer et al 2000). Hence, there are golden opportunities for uncovering comparatively unusual image configurations.

Section 2 provides an introduction to the lensing properties of scale-free galaxies with flat rotation curves. ^{*} We show that the caustic network, together with the locations of the cusps, can be worked out exactly. Section 3 considers two simple and very familiar models, namely those with elliptic isophotes and elliptic equipotentials (e.g., Kassiola & Kovner 1993). Such models, if acting as isolated lenses, are unable to produce higher order imaging. Section 4 identifies the physical causes of higher order imaging in terms of deviations of the isophotal shapes of the lensing galaxy from pure ellipses. Simple models are provided for lenses with boxy, disk and squarish isophotes and the onsets of sextuple and octuple imaging are calculated analytically. Finally, Section 5 concludes with a discussion of the frequency with which such higher order image systems occur, together with an assessment of forthcoming observational opportunities.

2 SCALE-FREE MODELS WITH FLAT ROTATION CURVES

2.1 Mass and Potential

Scale-free galaxy models with flat rotation curves are widely used in galactic astronomy and dynamics (e.g., Toomre 1982; Evans 1993; Evans, Carollo & de Zeeuw 2000). The isophotes of a scale-free galaxy have the same shape at every radius. The isophotes are completely described by a *shape function* $G(\theta)$, which depends only on the position angle θ with respect to the major axis. In such galaxies, the convergence κ and deflection potential ϕ satisfy

$$\kappa = \frac{G(\theta)}{2r}, \quad \phi = rF(\theta), \quad (2)$$

where (r, θ) are familiar polar coordinates in the lens plane. The surface density falls off along any ray like the reciprocal of distance and so the three-dimensional density falls off like the inverse square of distance. The models are projections of axisymmetric and triaxial generalisations of the familiar

^{*} Such models are often called “isothermal” in the lensing literature. This is an unfortunate nomenclature, as the velocity distributions are not in general isothermal. We prefer to use the more cumbersome term “scale free galaxies with flat rotation curves” to describe this family of models. The circular velocity curve of the spherical and axisymmetric models is everywhere flat. For the triaxial models, the circular velocity curve is not strictly speaking defined. Nonetheless, the structure of velocity space (and hence the elliptic closed orbit in the principal plane on which any cold gas lies) is the same independent of position. Hence, these models too have everywhere flat rotation curves.

isothermal sphere. As $\nabla^2\phi = 2\kappa$ (see e.g., Schneider et al. 1992), it is straightforward to establish that

$$G(\theta) = F(\theta) + F''(\theta). \quad (3)$$

Given an arbitrary shape function $G(\theta)$, it is possible to solve (3) by the method of variation of the parameters (e.g., Bronshtein & Semendyayev 1998, section 3.3.1.3.4) to obtain

$$F(\theta) = \sin\theta \int_0^\theta G(\vartheta) \cos\vartheta \, d\vartheta - \cos\theta \int_{\frac{\pi}{2}}^\theta G(\vartheta) \sin\vartheta \, d\vartheta. \quad (4)$$

The deflection angle has components

$$\phi_x = - \int_{\frac{\pi}{2}}^\theta G(\vartheta) \sin\vartheta \, d\vartheta, \quad \phi_y = \int_0^\theta G(\vartheta) \cos\vartheta \, d\vartheta. \quad (5)$$

This equation relates the lensing properties of the galaxy directly to the shape of the isophotes $G(\theta)$.

2.2 Critical Curves and Caustics

For scale-free models with flat rotation curves, the magnification is simply related to the convergence via (e.g., Witt, Mao & Keeton 2000)

$$\det J = 1 - 2\kappa. \quad (6)$$

The critical curves are given by the vanishing of the Jacobian and so they have the polar equation

$$r = G(\theta) = F(\theta) + F''(\theta). \quad (7)$$

Let the Cartesian coordinates of the caustic be (ξ, η) . Then, the caustic is given through the lens equation as

$$\begin{aligned} \xi &= F''(\theta) \cos\theta + F'(\theta) \sin\theta, \\ \eta &= F''(\theta) \sin\theta - F'(\theta) \cos\theta. \end{aligned} \quad (8)$$

If we introduce polar coordinates (s, α) in the source plane, then the equations (8) become

$$s \cos(\theta - \alpha) = F''(\theta), \quad s \sin(\theta - \alpha) = F'(\theta). \quad (9)$$

By substituting (4) into (8), we obtain the result

$$\begin{aligned} \xi &= G(\theta) \cos\theta + \int_{\frac{\pi}{2}}^\theta G(\vartheta) \sin\vartheta \, d\vartheta, \\ \eta &= G(\theta) \sin\theta - \int_0^\theta G(\vartheta) \cos\vartheta \, d\vartheta. \end{aligned} \quad (10)$$

Although this equation is simple to derive, it is rather remarkable. For scale-free galaxies with flat rotation curves, the caustics can be computed by a simple quadrature for *any isophotal shape*. Generally speaking, in gravitational lensing it is very hard to establish the maximum number of images that can be generated by a given lens. Often, numerical searches are the only way of tackling such questions and they risk missing small but important domains of parameter space. By contrast, here the caustic network is directly available to us and the onset of sextuple and octuple imaging can be found exactly.

2.3 The Role of Cusps

The appearance of swallowtails or butterflies usually leads to areas in the source plane where 6 or more images are

possible. Knowledge about the position of cusps is therefore very important. Since the caustic is given by the parametric representation (8), it is straightforward to derive the cusp locations. At a cusp, the caustic stops and reverses direction, so that the derivative of the caustic coordinates with respect to the parameter must vanish:

$$\frac{d\xi}{d\theta} = G'(\theta) \cos \theta = 0, \quad \frac{d\eta}{d\theta} = G'(\theta) \sin \theta = 0. \quad (11)$$

Both equation can only vanish simultaneously if the common factor $G'(\theta)$ vanishes. Therefore, the location of the cusps θ_{cusp} is simply given by the equation $G'(\theta_{\text{cusp}}) = 0$. This fact is remarkable since usually the equation for the cusps is very complicated. The cusps can occur only at the turning points of the shape function, so they are related to the properties of the isophotes in a straightforward way for these models.

In models without higher order cusps – such as swallowtails and butterflies – the caustic only has 4 simple cusps or folds. If a galaxy model permits the occurrence of swallowtails or butterflies, then it can show sextuple or octuple imaging. The onset of swallowtails happens when the second derivative of the shape function vanishes as well, $G'(\theta_{\text{cusp}}) = G''(\theta_{\text{cusp}}) = 0$ (see Schneider et al. 1992; Keeton, Mao & Witt 2000) so the first non-zero derivative is the third. Similarly, the onset of butterflies happens when all of the first three derivatives of the shape function vanish, $G'(\theta_{\text{cusp}}) = G''(\theta_{\text{cusp}}) = G'''(\theta_{\text{cusp}}) = 0$, so the first non-zero derivative is the fourth.

The zeros for the cusps θ_{cusp} are related to the length of the caustic. For the length of the caustic, we may write

$$\begin{aligned} l_{\text{caustic}} &= \int_0^{2\pi} \sqrt{(\xi'(\theta))^2 + (\eta'(\theta))^2} d\theta = \int_0^{2\pi} |G'(\theta)| d\theta \\ &= 2 \sum_{i=1}^{n_{\text{cusp}}/2} |G(\theta_{\text{cusp},2i}) - G(\theta_{\text{cusp},2i-1})|. \end{aligned} \quad (12)$$

Finally, the area under the caustic can also be given

$$\begin{aligned} A_{\text{caustic}} &= \int_0^{2\pi} \xi(\theta) \eta'(\theta) d\theta \\ &= \int_0^{2\pi} d\theta \int_0^\theta d\psi G'(\theta) G'(\psi) \cos \theta \sin \psi. \end{aligned} \quad (13)$$

This holds good provided the caustic does not self-intersect.

2.4 Area and Mass

For the spherical case ($G(\theta) = \text{const}$), it is well known that the mass inside the Einstein ring is directly related to the Einstein radius by $M_E = \tau_E^2$ (cf. Schneider et al. 1992). The area enclosed by the Einstein ring (i.e. the area inside the critical curve) is related to the mass by $\pi M_{\text{crit.curve}} = A_{\text{crit.curve}}$. From an observational perspective, the relation becomes $\pi M_{\text{crit.curve}} = \Sigma_{\text{crit}} D_d^2 A_{\text{crit.curve}}$, where the area is measured in arcsec^2 and the critical surface mass density is given by

$$\Sigma_{\text{crit}} = \frac{c^2 D_s}{4\pi G D_d D_{ds}}. \quad (14)$$

Here, D_d , D_s and D_{ds} are the distance to the deflector, the distance to the source and the distance from the deflector

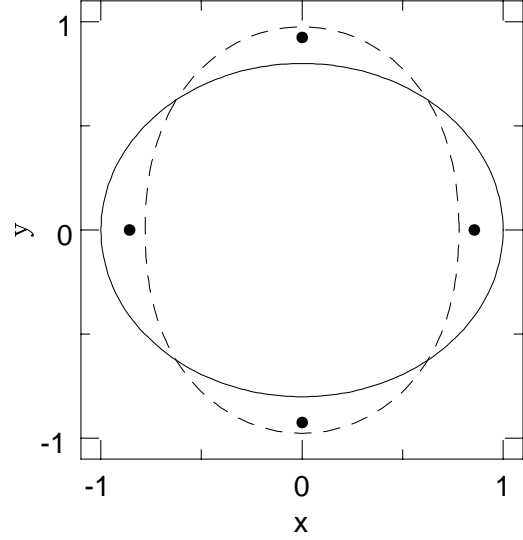


Figure 1. Critical curve (solid line) and reciprocal critical curve [as defined in eq. (17)] (dashed line) for an elliptical density distribution ($q = 0.8$) is shown. In both cases the mass inside the curve is proportional to the area, i.e. $A = \pi M$. The filled circles show the positions of the images when the source is located at the origin.

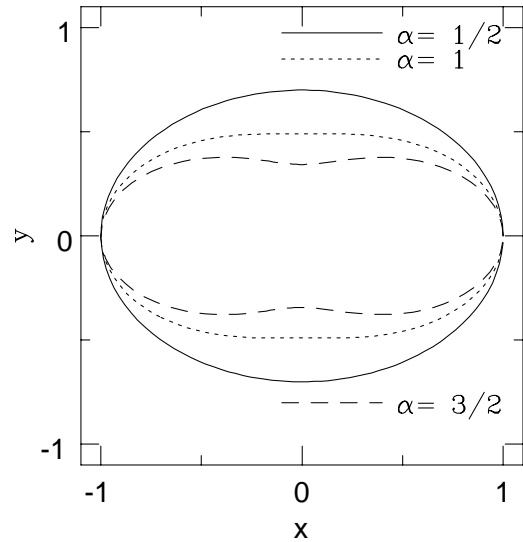


Figure 2. The isophotes of the family of models with shape function (25) with $q = 0.75$. Note that $\alpha = 0.5$ corresponds to elliptical isophotes, while $\alpha = 1.5$ corresponds to elliptical equipotentials. All these lenses are unable to show higher order imaging.

to the source respectively. Given the redshift of the lens and the source, this (14) enables the projected mass within the Einstein ring to be calculated for a spherical lens. In general, these useful relations do not remain valid for arbitrary, non-spherical lenses.

However, we now show that they do remain true for any scale-free potential obeying eq. (2). The mass within

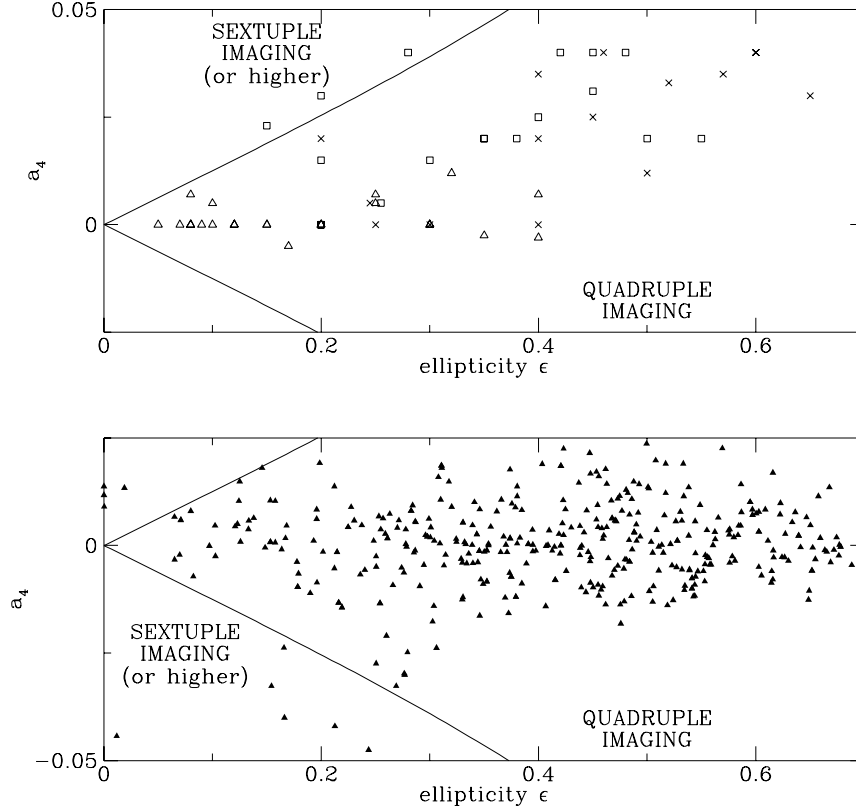


Figure 3. The onset of sextuple imaging as a function of the ellipticity of the isophotes ϵ and the parameter a_4 used to measure boxy and disk deviations. Upper panel additionally shows data from Saglia et al. (1993); triangles are elliptical galaxies, crosses are S0s and squares are SB0s in the Coma cluster. Lower panel additionally shows data from simulations of merger remnants by Heyl et al. (1994).

the critical curve is

$$\begin{aligned} M_{\text{crit. curve}} &= \frac{1}{\pi} \int_0^{2\pi} \int_0^{R(\theta)} \kappa(r, \theta) r dr d\theta \\ &= \frac{1}{2\pi} \int_0^{2\pi} G^2(\theta) d\theta. \end{aligned} \quad (15)$$

The area inside the critical curve is

$$A_{\text{crit. curve}} = \int_0^{2\pi} \int_0^{R(\theta)} r dr d\theta = \frac{1}{2} \int_0^{2\pi} G^2(\theta) d\theta, \quad (16)$$

where we have used eq. (7) for the dependency of the critical curve on the angle. So, we obtain again $\pi M_{\text{crit}} = A_{\text{crit}}$.

Many authors have suggested that the mass inside the ellipsoidal ring formed by the images of a quadruple lens is approximately constant, almost independent of the lens model; for example, the models of Kochanek (1991), Rix, Schneider & Bahcall (1994), Witt, Mao & Schechter (1995), Chae, Turnshek, & Khersonsky (1998) and Hunter & Evans (2001) for the Einstein Cross (Q2237+0305) are very different and predict different flux ratios for the 4 images, but they all agree on the projected mass within the central $0.9''$ enclosed by the images. We want to shed some light on this issue! Let us define *the reciprocal critical curve* as

$$R(\theta) = c/r_{\text{crit. curve}} = c/G(\theta). \quad (17)$$

The mass inside the reciprocal critical curve is

$$M_{\text{recip. curve}} = \frac{1}{\pi} \int_0^{2\pi} \int_0^{R(\theta)} \kappa(r, \theta) r dr d\theta = c, \quad (18)$$

and it too must remain constant. Let us choose the constant c in such a way that the area inside the reciprocal critical curve $A_{\text{recip. curve}}/\pi = c$ is proportional to the mass, obtaining

$$c = \frac{2\pi}{\int_0^{2\pi} G^{-2}(\theta) d\theta}. \quad (19)$$

As shown in Figure 1, we can imagine that the images are confined by the critical curve and the reciprocal critical curve. If the source position is closer to the caustic, then the images are located closer to the critical curve. In other cases, the images may be closer to the reciprocal critical curve. The image positions follow (approximately) the critical curve or the reciprocal critical curve. The area within the critical and inverse critical curves is directly proportional to enclosed mass. Hence, to a good approximation, the area enclosed by the four images is as well. (Small deviations might arise due to the interpolation curve $R(\theta)$ chosen to connect the images of the quadruplet).

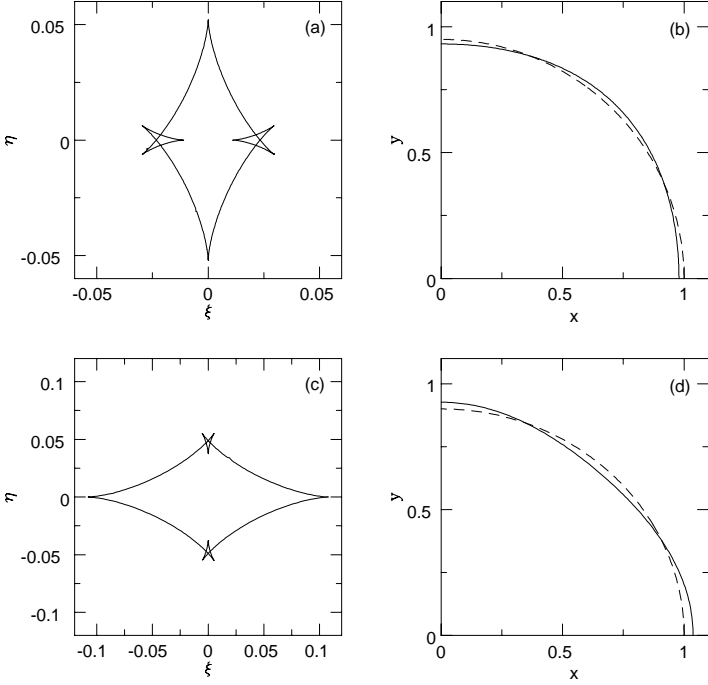


Figure 4. The caustic network and isophote shape for elliptical galaxy models with (a,b) boxy and (c,d) disk isophotes. Butterfly caustics appear on respectively the major and minor axes projected onto the source plane. A pure elliptical isophote is shown for comparison in dotted lines, so that the boxy and disk isophotal deviations can be discerned. [Panels (a,b) are for a model with $\epsilon = 0.05$ and $a_4 = -0.02$, panels (c,d) are for $\epsilon = 0.1$ and $a_4 = 0.03$].

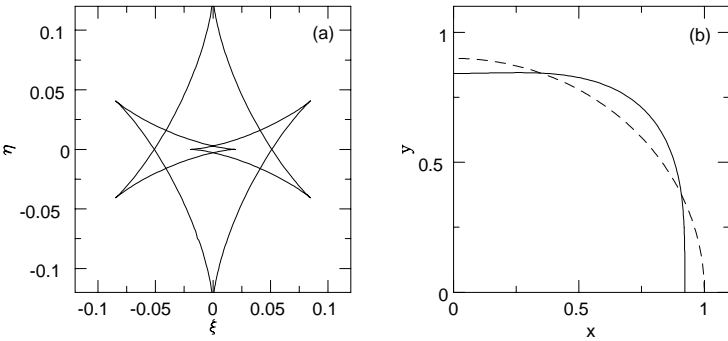


Figure 5. As the distortion increases, the butterfly cusps merge. If the source lies in the region where the two caustics overlap, then eightfold imaging occurs. [This shows a model with $\epsilon = 0.1$ and $a_4 = -0.075$].

3 SIMPLE MODELS

3.1 Elliptic Isophotes and Equipotentials

There are two very familiar models that fall into the class of scale-free galaxies with flat rotation curves. The first has

elliptic isophotes, so that the shape function is

$$\begin{aligned} G(\theta) &\propto \left(\frac{1}{2}(1+q^{-2}) + \frac{1}{2}(1-q^{-2})\cos 2\theta \right)^{-\frac{1}{2}}, \\ &\propto \left(\cos^2 \theta + q^{-2} \sin^2 \theta \right)^{-\frac{1}{2}}. \end{aligned} \quad (20)$$

It is easy to find the deflection potential as

$$\phi = x\phi_x + y\phi_y, \quad (21)$$

with

$$\begin{aligned} \phi_{,x} &= - \int_{\frac{\pi}{2}}^{\theta} G(\vartheta) \sin \vartheta d\vartheta \\ &= \frac{q}{\sqrt{1-q^2}} \tan^{-1} \left(\sqrt{\frac{1-q^2}{q^2 \cos^2 \theta + \sin^2 \theta}} \cos \theta \right), \\ \phi_{,y} &= \int_0^{\theta} G(\vartheta) \cos \vartheta d\vartheta \\ &= \frac{q}{\sqrt{1-q^2}} \tanh^{-1} \left(\sqrt{\frac{1-q^2}{q^2 \cos^2 \theta + \sin^2 \theta}} \sin \theta \right) \end{aligned} \quad (22)$$

This result has been given before (see e.g., Kassiola & Kovner 1993; Kormann, Schneider, Bartelmann 1994). By explicit construction, Keeton et al. (2000) showed that an elliptical density distribution plus external shear can provide 6 or 8 images configurations. This happens when the external shear is strong and aligned along the minor axis of the lensing galaxy.

The second has elliptic equipotentials, so that

$$\begin{aligned} F(\theta) &\propto \sqrt{\frac{1}{2}(1+q^{-2}) + \frac{1}{2}(1-q^{-2})\cos 2\theta} \\ &\propto \sqrt{\cos^2 \theta + q^{-2} \sin^2 \theta}. \end{aligned} \quad (23)$$

This model was introduced into lensing by Blandford & Kochanek (1987) and subsequently studied by others (e.g., Witt 1996; Witt & Mao 1997, 2000; Hunter & Evans 2001). The three dimensional analogues of these models are well-known in galactic dynamics as power-law galaxies (Evans 1993, 1994). It is straightforward to find the shape function as

$$G(\theta) \propto q^{-2} \left(\frac{1}{2}(1+q^{-2}) + \frac{1}{2}(1-q^{-2})\cos 2\theta \right)^{-\frac{3}{2}}. \quad (24)$$

On geometric grounds, it seems likely that an elliptically stratified potential plus external shear cannot have more than 4 (or 5) images. The reason for this is the confinement of the image positions. As found by Witt (1996) and Witt & Mao (1997), the 4 (or 5) images of an elliptical potential are constrained to lie on a hyperbola. If any new image pairs appear, they must also lie on this hyperbola. Physically, we expect that each new image pair is located close to the Einstein ring. Since a hyperbola can have at most only 4 intersection points with a ring-like curve, it is intuitively clear that an elliptical potential plus shear may not have more than 4 images (or 5 images if there is additionally one close to the centre of the lensing galaxy). An analytical proof of the maximum number of images for power-law galaxies with elliptic equipotentials is provided in Appendix A of Hunter & Evans (2001).

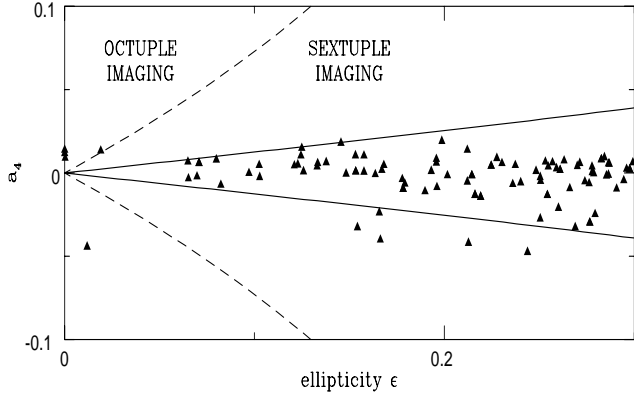


Figure 6. The onset of octuple imaging as a function of the ellipticity of the isophotes ϵ and the parameter a_4 used to measure boxy and disky deviations. Data from simulations of merger remnants by Heyl et al. (1994) are overplotted.

3.2 Number of Images

Both these simple models are members of a more general class that have a shape function $G(\theta)$ of the form:

$$G(\theta) \propto \left(\frac{1}{2}(1+q^{-2}) + \frac{1}{2}(1-q^{-2})\cos 2\theta \right)^{-\alpha}, \quad (25)$$

where α is constant. Figure 2 shows isophotes for three members of the family, namely $\alpha = 1/2$ (elliptic isophotes), $\alpha = 1$ and $\alpha = 3/2$ (elliptic equipotentials). For the same q , the models become flatter with increasing α . The isophotes can become “peanut-shaped”; this is valuable for modelling the peanut-shaped bulges of spiral galaxies (see e.g., Shaw 1987, Bureau & Freeman 1999).

The positions of the cusps are found by solving $G'(\theta) = 0$ and so

$$\theta_{\text{cusp}} = \frac{n\pi}{2}, \quad n = 0, 1, 2, 3. \quad (26)$$

It is straightforward to establish

$$G''(\theta_{\text{cusp}}) \propto (1-q^{-2}) [1+q^{-2} + (-1)^n(1-q^{-2})]^{-\alpha-1}. \quad (27)$$

For flattened models ($q \neq 1$), this never vanishes and so higher order cusps like swallowtails never occur. This provides a simple proof that scale-free galaxies with flat rotation curves and elliptic isophotes or equipotentials have at most 4 (or 5) images depending on the density singularity at the centre. Of course, the proof is slightly more general, holding good for all models with shape functions of form eq (25).

4 ISOPHOTAL DEVIATIONS

The isophotes of elliptical galaxies are well approximated by pure ellipses. Observers typically measure deviations from ellipses of the order of a few percent. This might betray the presence of an embedded disk or a central bar. Boxy or irregular isophotes may be caused by recent merging and interaction. Typically the difference between the isophote r_i and a reference ellipse r_e is expanded as a Fourier series (e.g., Binney & Merrifield 1998)

$$r_i - r_e = \frac{a_0}{2} + \sum_{n=1}^{\infty} a_n \cos n\theta + b_n \sin n\theta, \quad (28)$$

Provided the reference ellipse has been well-chosen, the Fourier coefficients are all small. The largest non-vanishing components are usually a_4 (which is a measure of boxiness and diskiness) and b_4 (which is a measure of skewness and squareness). The a_3 and b_3 coefficients are significant only in elliptical galaxies with dust lanes. Observers normalise the Fourier coefficients to the semimajor axis of the reference ellipse. Henceforth, we always use normalised Fourier coefficients, so that our models are directly comparable to the data.

4.1 Boxiness and Diskiness

Boxiness and diskiness has been of interest ever since Bender et al. (1989) pointed out possible correlations of the a_4 parameter with X-ray, radio and kinematic properties. This correlation remains poorly understood, especially as the boxiness and diskiness is partly a function of the inclination angle of the galaxy (Franx 1988). The flattest galaxies have the largest values for $|a_4|$. In fact, galaxies with an ellipticity greater than 0.35 almost always have $|a_4| > 0.005$ (Bender et al. 1989). Approximately one third of elliptical galaxies show boxiness at the level $a_4 < -0.005$, one third show diskiness at the level $a_4 > 0.005$ and one third show deviations of $|a_4| < 0.005$. Values of $|a_4|$ much in excess of 0.05 are uncommon for normal ellipticals.

We study the shape function is

$$G(\theta) \propto \left[\frac{1}{2}(1+q^{-2}) + \frac{1}{2}(1-q^{-2})\cos 2\theta - A \cos 4\theta \right]^{-\frac{1}{2}}. \quad (29)$$

When A vanishes, the model reduces to (20). Otherwise, if $A > 0$, then the model has disky isophotes, while if $A < 0$ then the model has boxy isophotes. Observers typically record the isophote shape in terms of the ellipticity $\epsilon = 1 - q$ and the Fourier coefficient a_4 . In the limit of small deviations, A is related to the observables through the equation

$$a_4 = \frac{A}{32}(4-3\epsilon)^2 + O(\epsilon^4, A^2). \quad (30)$$

These models can exhibit butterfly cusps at surprisingly small deviations. The condition for butterflies is $G'(\theta_{\text{cusp}}) = G''(\theta_{\text{cusp}}) = G'''(\theta_{\text{cusp}}) = 0$, so that the first non-vanishing derivative is the fourth. This is satisfied at or beyond the critical value

$$|A_{\text{crit},6}| = \frac{1}{8}(1-q^{-2}). \quad (31)$$

This condition can be re-written in terms of the observational parameters a_4 and ϵ as

$$|a_4| \gtrsim \frac{1}{256} \frac{\epsilon(4-3\epsilon)^2(2-\epsilon)}{(1-\epsilon)^2}. \quad (32)$$

This marks the onset of sextuple imaging.

In Figure 3, the boundary between quadruple and sextuple imaging is shown in solid lines. In the upper panel, we also plot the data of Saglia, Bender & Dressler (1993) on a total of 58 elliptical galaxies, S0s and SB0s in the Coma cluster. In the lower panel, we plot the data on isophotal shapes of 424 merger remnants from simulations by Heyl, Hernquist & Spergel (1994). There are a number of things to notice.

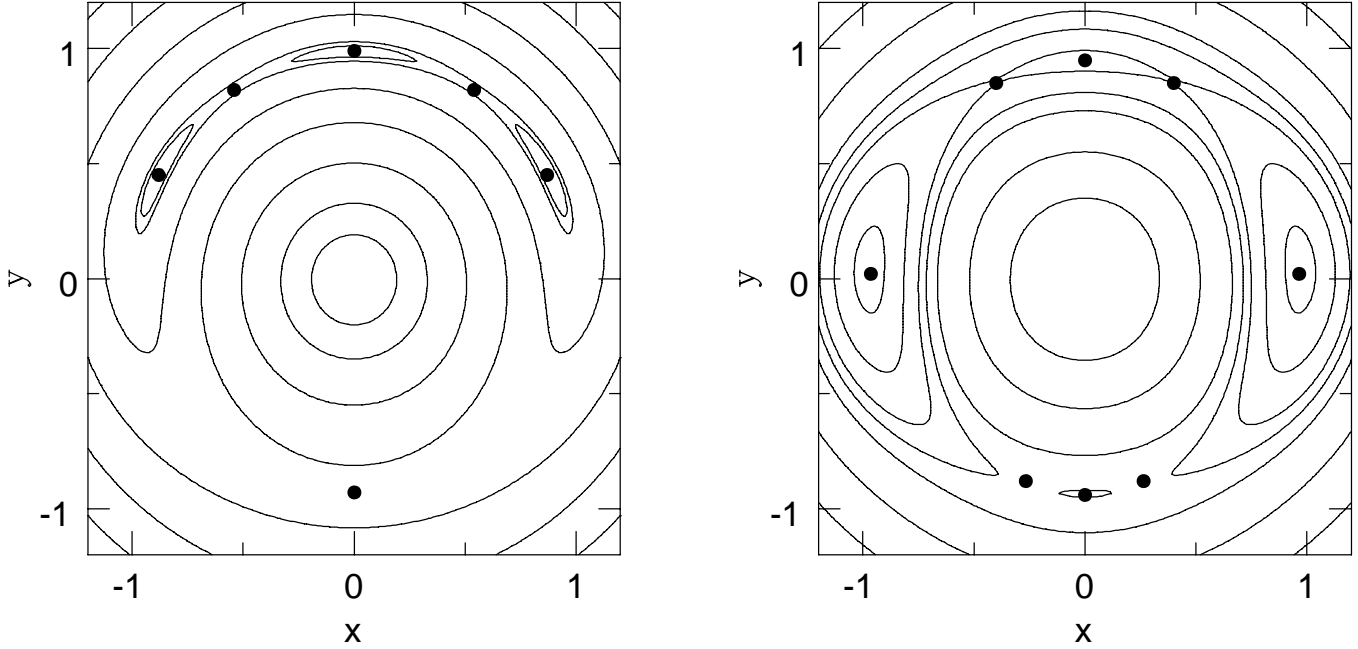


Figure 7. The topology of the Fermat surfaces for instances of (left panel) sextuple and (right panel) octuplet imaging. The even parity images are located at the minima of the Fermat surface, the odd parity images at the saddle points. Image locations are marked with filled circles. [The left panel corresponds to the model shown in Figure 4(a) with source position $\xi = 0.02, \eta = 0.0$. The right panel corresponds to the model shown in Figure 5(a) with source position $\xi = 0.005, \eta = 0.0$].

First, very small values of $|a_4|$ suffice to produce sextuple imaging, if the galaxy is quite round. However, nearly round galaxies tend to have very small deviations from the pure elliptical form. Second, all the elliptical galaxies in Saglia et al.'s (1993) sample lie in the quadruple imaging domain. The possibilities for sextuple imaging improve for S0 and especially SB0 galaxies. Saglia et al.'s sample contains only galaxies for which a stable value of a_4 can be derived from the photometry and does not include galaxies which exhibit isophote twisting or those which show boxiness and diskiness in the same isopotential contours. So, it probably underestimates the frequency with which substantial deviations from pure ellipses occur. Nonetheless, out of a total of 58 galaxies, 3 have the potential for sextuple imaging. Third, the merger remnants of Heyl et al. (1994) are typically boxy. This though is a rough rule-of-thumb, as some can appear diskly. We see that 10 out of the total of 424 simulated merger remnants are irregular enough to permit sextuple imaging or higher. Bearing in mind that most of the lensing optical depth is in early-type galaxies, we reckon that the fraction of lenses that have the ability to cause sextuple imaging or higher is $\sim 3\%$.

Figure 4 shows the caustic networks for two models. The upper panels refer to a model which has ellipticity $\epsilon = 0.05$ and boxy isophotes with $a_4 = -0.02$. The lower panels refer to a model which has $\epsilon = 0.1$ and diskly isophotes with $a_4 = 0.03$. The locations of the cusps are given by the equations

$$\sin 2\theta_{\text{cusp}} = 0 \quad \text{and} \quad \cos 2\theta_{\text{cusp}} = \frac{1 - q^{-2}}{8A}. \quad (33)$$

This means that the 4 cusps remain on the major and minor axes with increasing distortion A , but 4 additional cusps appear as soon as the critical value $A_{\text{crit},6}$ is exceeded. Note the butterfly cusps develop on the major axis in the boxy case, and on the minor axis in the diskly case. If the source lies within the butterfly caustic, then it is lensed into six images.

The butterfly cusps touch at the onset of octuplet imaging. Figure 5 shows an example when the butterfly cusps have merged. A source in the overlapping region will be lensed into eight images. The isophote shape is now very rectangular, but examples of such galaxies are known (see, for example, NGC 128 as pictured in Burbidge & Burbidge 1959). The critical value of the distortion $A_{\text{crit},8}$ required for eightfold imaging is given by solution of the implicit equation

$$\int_0^{\frac{\pi}{2}} \frac{d\vartheta \cos \vartheta}{\left[\frac{1}{2}(1+q^{-2}) + \frac{1}{2}(1-q^{-2}) \cos 2\vartheta - |A_{\text{crit},8}| \cos 4\vartheta\right]^{\frac{1}{2}}} = \frac{1}{\sqrt{q^2 - |A_{\text{crit},8}|}}. \quad (34)$$

As the distortion is always small, we can linearise this equation and solve it to obtain

$$|A_{\text{crit},8}| \approx \frac{2(I_1 - q)}{q^3 - I_2}. \quad (35)$$

This marks the onset of octuplet imaging. The integrals I_1

and I_2 are

$$\begin{aligned}
 I_1 &= \int_0^{\frac{\pi}{2}} \frac{\cos \vartheta d\vartheta}{\left[\frac{1}{2}(1+q^{-2}) + \frac{1}{2}(1-q^{-2})\cos 2\vartheta\right]^{\frac{3}{2}}}, \\
 &= \frac{q}{\sqrt{1-q^2}} \tanh^{-1} \sqrt{1-q^2}, \\
 I_2 &= \int_0^{\frac{\pi}{2}} \frac{\cos \vartheta \cos 4\vartheta d\vartheta}{\left[\frac{1}{2}(1+q^{-2}) + \frac{1}{2}(1-q^{-2})\cos 2\vartheta\right]^{\frac{3}{2}}}, \\
 &= q[q^4 + 10q^2 + 1 - 4q(2+q^2)I_1]/(1-q^2)^2. \quad (36)
 \end{aligned}$$

They can be evaluated numerically easily enough. Figure 6 shows the distortion required for octuple imaging in the plane of the observables. Overplotted is the simulation data of Heyl et al. (1994), from which it is clear that 5 of the merger remnants are sufficiently distorted to permit even eightfold imaging.

Figure 7 shows contours of the Fermat potential

$$\psi(x, y, \xi, \eta) = \frac{1}{2}|(x - \xi)^2 + (y - \eta)^2| - \phi(x, y), \quad (37)$$

for typical 6 image and 8 image configurations. Let us recall that the Fermat potential is proportional to the time delay (e.g., Schneider et al. 1992). The left panel shows the model of Figure 4(a) with the source placed within the butterfly cusp so that it has 6 images (3 of even parity corresponding to the minima of the Fermat surface, 3 of odd parity corresponding to the saddle points). The right panel shows the model of Figure 5(a) with the source placed in the region of overlap of the butterfly cusps, so that there are now 8 images, 4 of even parity and 4 of odd parity. Notice that all the images are at roughly the same distance from the centre of the lensing galaxy. In fact, the arrangement has obvious similarities with the deep *Hubble Space Telescope* images of CL0024+1654, which comprises 8 images of a single blue galaxy lensed by a foreground cluster (Tyson, Kochanski & Dell'Antonio 1998), as well as the incomplete optical Einstein ring 0047-2808, which is the image of a high redshift early-type star-forming galaxy (Warren et al. 1999).

Scale-free models with flat rotations have another elegant and unusual property. The relative time delay between the i th and j th image is simply related to the radial positions r_i and r_j via (Witt et al. 2000; see also Koopmans, de Bruyn & Jackson 1998; Zhao & Pronk 2001)

$$\Delta t_{i,j} = \frac{D_d D_s}{2cD_{ds}} (1 + z_d)(r_j^2 - r_i^2), \quad (38)$$

where z_d is the redshift of the deflector. Sextuple and octuple image systems typically have all the images in a ring-like configuration and so the relative time delays between any of the pairs is never very large.

4.2 Skewed Squarishness

Photometric studies of elliptical galaxies find that the other Fourier coefficient that is typically non-zero is b_4 (e.g., Franx, Illingworth & Heckman 1989). To study its effect, we examine the shape function

$$G(\theta) \propto \left[\frac{1}{2}(1+q^{-2}) + \frac{1}{2}(1-q^{-2})\cos 2\theta - B \sin 4\theta\right]^{\frac{1}{2}}, \quad (39)$$

where without loss of generality $B \geq 0$. If the distortion B is non-vanishing, then the isophotes become skewed and squarish. This may be useful for modelling face-on bars in

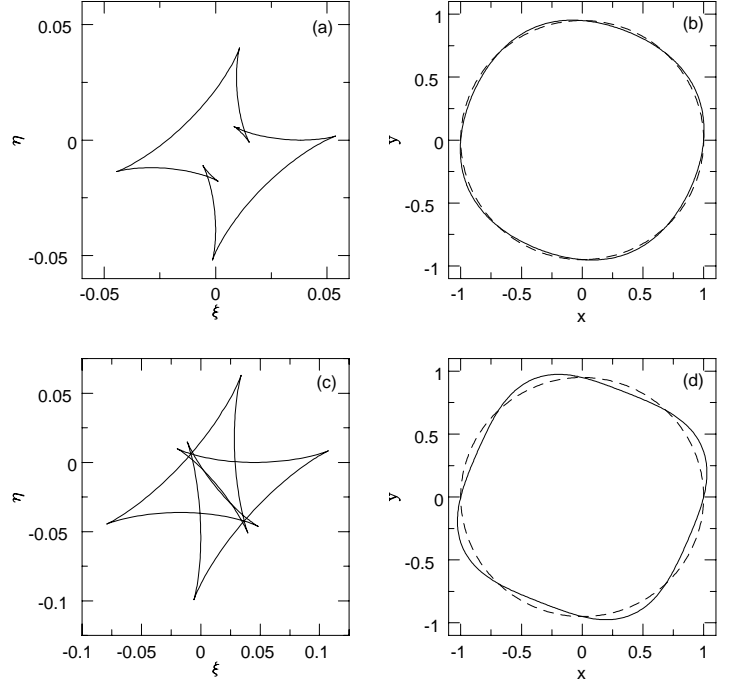


Figure 8. The caustic network and isophote shape for galaxies with the shape function (39). Again, pure elliptical isophotes are shown in dotted lines for comparison. Both models have swallowtail cusps. [Panels (a,b) are for a model with $\epsilon = 0.05$ and $b_4 = 0.02$, panels (c,d) are for $\epsilon = 0.05$ and $b_4 = 0.06$].

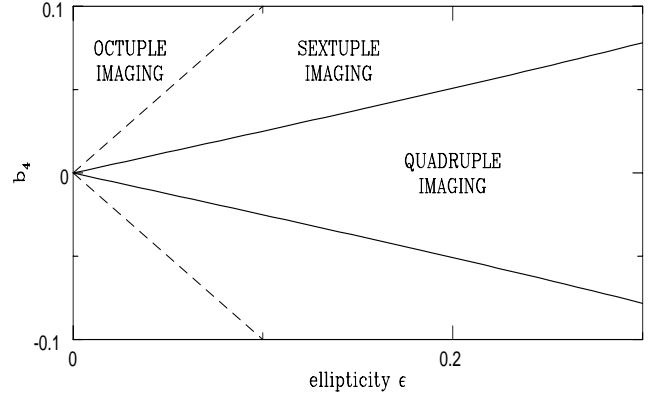


Figure 9. The onset of sextuple imaging as a function of the ellipticity of the isophotes ϵ and the parameter b_4 used to measure skewed squarishness.

spiral disks, rather like the lensing galaxy for Q2237+0305 (the Einstein Cross). The observables are the ellipticity $\epsilon = 1 - q$ and the Fourier coefficient b_4 , which is

$$b_4 = \frac{B}{32}(4 - 3\epsilon)^2 + O(\epsilon^4, B^2). \quad (40)$$

Unlike a_4 , the sign of b_4 carries no physical significance and can be inverted by a simple reflection. Observationally speaking, the b_4 coefficient is usually, but not always, smaller

than a_4 (see e.g., Franx et al. 1989). The b_4 coefficient has received less attention than a_4 , as it does not appear to be correlated with radio or X-ray properties. There are no extensive tables of data on b_4 available in the literature. Nonetheless, individual galaxies with b_4 as large as 0.05 are known, such as NGC 1700 (Franx et al. 1989).

The condition for swallowtails is $G'(\theta_{\text{cusp}}) = G''(\theta_{\text{cusp}}) = 0$, so that the first non-vanishing derivative is the third. This is satisfied whenever B exceeds the critical value given

$$B_{\text{crit},6} = \pm \frac{1}{4}(1 - q^{-2}). \quad (41)$$

Again, it is useful to rewrite this in terms of the observables as

$$b_4 \approx \frac{1}{128} \frac{\epsilon(4 - 3\epsilon)^2(2 - \epsilon)}{(1 - \epsilon)^2}. \quad (42)$$

This marks the onset of sextuple imaging.

Figure 8 shows the caustic network for a case when the swallowtails have just developed ($\epsilon = 0.05$ and $b_4 = 0.02$), together with a case in which the swallowtails have overlapped to create a domain in the source plane where eightfold imaging occurs ($\epsilon = 0.05$ and $b_4 = 0.06$). The cusps occur at the locations

$$\sin 2\theta = \frac{1 - q^{-2}}{16B} \pm \sqrt{\frac{(1 - q^{-2})^2}{256B^2} + \frac{1}{2}}. \quad (43)$$

The cusps move further away from the major and minor axes for increasing distortion B . We obtain 4 additional cusps when the swallowtails form as B reaches the critical value $B_{\text{crit},6}$. This happens at the angular locations $\theta_{\text{cusp}} = \frac{\pi}{4}(2n + 1)$, where n is an integer. If the distortion B increases still further, then the swallowtails can overlap. This is when eightfold imaging becomes possible. The critical value $B_{\text{crit},8}$ can be determined by requiring that the two inner pair of cusps just touch each other. Let us label the cups in Figure 8 in numerical order counterclockwise starting with 1 on the extreme right hand side. Then, the condition can be expressed as $\xi(\theta_{\text{cusp},2}) = \xi(\theta_{\text{cusp},7})$ and $\eta(\theta_{\text{cusp},2}) = \eta(\theta_{\text{cusp},7})$. Simultaneously, the 6th and 8th cusps touch each other as well. The onset of octuple imaging can be calculated analytically, but it is rather cumbersome and so we resort to the computer.

Figure 9 shows the domains in which sextuple and octuple imaging is possible as a function of the ellipticity ϵ and the Fourier coefficient b_4 . Unfortunately, tables of data of b_4 are not available, although b_4 is typically smaller than a_4 and rarely exceeds 0.05. On comparing Figure 9 to the earlier Figures 3 and 6, we see that the skewed squarishness is less efficient at causing higher order imaging than diskiness or boxiness.

5 CONCLUSIONS

Many sextuple or octuple images of multiply lensed quasars are likely to exist. If a galaxy with a flat rotation curve has exactly elliptical isophotes, then it yields at most 4 or 5 images (depending on the behaviour of the convergence or surface density at the centre). Higher order imaging is caused by deviations of the isophotes from pure elliptical form, such as

boxiness or diskiness. Even isolated boxy or disky elliptical galaxies provide caustic networks with swallowtail and butterfly cusps and so permit sixfold or eightfold imaging if the source is located propitiously. The rounder the lensing galaxy, then the smaller the distortion of the isophotes required. The criteria for the onset of sextuple and octuple imaging can be given exactly in terms of the ellipticity ϵ and the Fourier coefficients a_4 and b_4 used by observers to measure deviations such as boxiness, diskiness and skewed squarishness (see eqs. 32, 35, 42).

The first examples of galaxy models that can produce sextuple or octuple images were found by Witt & Mao (2000) and Keeton et al. (2000). These models have elliptical density contours with the external shear perpendicular to the flattening. These are rare cases, as they require large values of the external shear for the cross-section to be substantial – larger than typically provided by the effects of large-scale structure. So, one must be lucky to observe higher order imaging produced by such configurations. Six and eight image configurations can also occur when multiple galaxies lie at the same redshift (Keeton et al. 2000) or at distinct redshifts (Chae, Mao & Augusto 2001). This may be quite common, as the lens in the 6 image case found by Rusin et al (2001) seems to be a cluster. However, it is perhaps less surprising that groups of galaxies can produce unusual image configurations.

A crude estimate suggests that about 3% of the lensing galaxy population has the potential to produce sextuplets or octuplets. Unfortunately, the cross-sectional area in the source plane producing sextuple imaging is approximately a factor of 10 times smaller than that producing quadruple. However, the probability of observing a sextuplet is increased by a factor of ~ 5 by the magnification bias (see e.g. Turner 1980; Turner, Ostriker & Gott 1984). Therefore, a realistic estimate is that sextuple and octuple images comprise $\sim 1\%$ of all multiply imaged systems. Note that we have ignored galaxies that show isophote twisting (e.g., Bertola 1981) and galaxies which exhibit boxiness and diskiness in the same isophotal contours (e.g., Nieto & Bender 1989). We have also not included the contribution from multiple lensing by groups of galaxies. These might be expected to augment the numbers of sextuplets and octuplets, and so we reckon our estimate errs on the side of pessimism.

It is reasonable to expect that both the Next Generation Space Telescope (NGST; see e.g. Barkana & Loeb 2000) and the Global Astrometric Interferometer for Astrophysics (GAIA; see e.g., de Boer et al. 2000) will discover such configurations. For example, GAIA is the ESA satellite now selected as a Cornerstone 6 mission as part of the Science Program [†]. It is an all-sky survey satellite that provides multi-colour, multi-epoch photometry, astrometry and radial velocities on all objects brighter than $V \approx 21$ (e.g., de Boer et al. 2000). It will be sensitive to multiply-imaged quasars with separations as small as $\sim 0.2''$. It is crudely estimated that GAIA will detect ~ 4000 multiply-imaged quasars. In a dataset of such size, we expect ~ 40 sextuple or octuple image systems. Both NGST and GAIA will also find “mini” Einstein rings. We expect that, in many cases,

[†] <http://astro.estec.esa.nl/SA-general/Projects/GAIA/gaia.html>

some of the six or eight images will be merged to form arcs. On account of the magnification bias, we expect the lenses to be typically high redshift galaxies and so the sources themselves will have redshift $\gtrsim 2$. Therefore, GAIA should also find “mini” Einstein rings, where the diameter of the ring is sub-arcsecond.

It is interesting to note that any additional cusps produced by distortion or deviation of elliptical symmetry increases the magnification of the quadruple image configurations as well. It is still a puzzle why we observe so many quadruplets. Simulations typically predict many more double than quadruple image systems. Boxy or disky elliptical galaxies favour the occurrence of more quadruplets. This is because the magnification of the 4 images is increased by the appearance of additional cusps inside the 4 image régime. This fact has been neglected as only highly symmetric galaxy models have been typically used in numerical simulations.

The boxy and disky galaxy models with flat rotation curves introduced in this paper are a natural extension of the popular and widely-used elliptic density models. They have many attractive properties. The critical curves and the relative time delays are analytic. The deflection angles and the caustics are simple quadratures and so easily evaluated. The lens equation can be reduced to a one-dimensional equation, and so the image positions can be found numerically without recourse to grid searching algorithms. Boxy and disky galaxy models provide new opportunities to remodel observed quadruple lenses, where existing models have proved unable to calculate the flux ratio of the images correctly. A good candidate might be MG0414+0534 (see e.g. Hewitt et al. 1992). Here, we have 4 radio images with well-determined flux ratios; however, no model has so far been able to reproduce the flux ratios satisfactorily (Falco, Lehar & Shapiro 1997). The most recent attempt (Trotter, Winn & Hewitt 2000) concludes that the lensing galaxy is somewhat quadrangular and boxy.

ACKNOWLEDGMENTS

We thank Shude Mao and Stephen Warren for a number of interesting discussions and Jeremy Heyl for kindly providing us with data from his simulations. NWE is supported by the Royal Society. HJW acknowledges the hospitality of the sub-Department of Theoretical Physics during working visits.

REFERENCES

Barkana R., Loeb A. 2000, ApJ, 531, 613
 Bender R., Surma P., Doebereiner S., Moellenhoff C., Madejsky R., 1989, A&A, 217, 35
 Bertola F., 1981, In “Structure and Evolution of Normal Galaxies”, eds. S.M. Fall, D. Lynden-Bell, (Cambridge University Press: Cambridge), p. 13
 Binney J.J., Merrifield M., 1998, Galactic Astronomy, Princeton University Press, Princeton
 Blandford R., Kochanek C., 1987, ApJ, 321, 658
 de Boer K.S., Gilmore G., Hog E., Lattanzi M.G., Lindegren L., Luri X., Mignard F., de Zeeuw P.T. 2000, GAIA: Composition, Formation and Evolution of the Galaxy, ESA-SCI(2000)4

Bronstein I.N., Semendyayev K.A., 1998, Handbook of Mathematics (Springer-Verlag, New York)
 Burbidge E.M., Burbidge G., 1959, ApJ, 130, 20
 Bureau M., Freeman K.C., 1999, AJ, 118, 126
 Burke W., 1981, ApJ, 244, 1
 Chae K.H., Mao S., Augusto P., 2001, MNRAS, in press (astro-ph/0104467)
 Chae K.H., Turnshek D.A., & Khersonsky V.K. 1998, ApJ, 495, 609
 Chen G.H., Hewitt J.N., 1993, AJ, 106, 1719
 Colley W.N., Tyson J.A., & Turner E.L. 1996, ApJ, 461, L83
 Evans N.W., 1993, MNRAS, 260, 191
 Evans N.W., 1994, MNRAS, 267, 333
 Evans N.W., Wilkinson M.I., 1998, MNRAS, 296, 800
 Evans N.W., Carollo M., de Zeeuw P.T., 2000, MNRAS, 318, 1131
 Falco E., Lehar J., Shapiro I., 1997, AJ, 113, 540
 Franx M., 1988, Ph.D. thesis, Leiden University
 Franx M., Illingworth G.D., Heckman T., 1989, AJ, 98, 538
 Hewitt J.N., Turner E.L., Lawrence C.R., Schneider D.P., & Brody J.P. 1992, AJ, 104, 968
 Heyl J.S., Hernquist L., Spergel D.N., 1994, ApJ, 427, 165
 Hunter C., Evans N.W., 2001, ApJ, 554, 1227
 Iбата R., Lewis G.F., Irwin M.J., Lehar J., Totten E., 1999, AJ, 118, 1922
 Kassiola A., Kovner I., 1993, ApJ, 417, 450
 Keeton C.R., Mao S., Witt H.J., 2000, ApJ, 537, 697
 Kochanek C.S. 1991, ApJ, 373, 354
 Koopmans L.V.E., de Bruyn A.G., Jackson N. 1998, MNRAS, 295, 534
 Kormann R., Schneider P., Bartelmann M., 1994, A&A, 284, 285
 Myers S.T. et al., 1995, ApJ, 447, L5
 Myers S.T., 1999, Proc. Natl. Acad. Sci., 96, 4236
 Nieto J.L., Bender R., 1989, A&A, 215, 266
 Pospieszalka A., et al. 1999, in “Gravitational Lensing: Recent Progress and Future Goals”, eds T.G. Brainerd, C.S. Kochanek, ASP Conf. Ser., in press
 Rix, H-W., Schneider D.P., Bahcall J.N. 1992, AJ, 104, 959
 Rusin D., Kochanek C.S., Norbury M. Falco E.E., Impey C.D., Lehar J., McLeod B.A., Rix H-W., Keeton C.R., 2001, ApJ, in press (astro-ph/0011505)
 Saglia R.P., Bender R., Dressler A., 1993, A&A, 279, 75
 Schneider P., Ehlers J., Falco E.E., 1992, Gravitational Lenses (Springer-Verlag, New York)
 Shaw M., 1987, MNRAS, 229, 691
 Toomre A., 1982, ApJ, 259, 535
 Trotter C.S., Winn J.N., Hewitt J.N., 2000, AJ, 535, 671
 Turner E.L. 1980, ApJ, 242, L135
 Turner E.L., Ostriker J.P., Gott J.R. 1984, ApJ, 284, 1
 Tyson J.A., Kochanski G.P., dell’Antonio I.P. 1998, ApJ, 498, L107
 Warren S.J., Lewis G.F., Hewitt P.C., Møller P., Shaver P., Iovino, A. 1999, A&A, 343, L35
 Witt H.J., 1996, ApJ, 472, L1
 Witt H.J., Mao S., 1997, MNRAS, 291, 211
 Witt H.J., Mao S., 2000, MNRAS, 311, 689
 Witt H.J., Mao S., Keeton C.R., 2000, ApJ, 544, 98
 Witt H.J., Mao S., Schechter P.L. 1995, ApJ, 443, 18
 Zhao H.S., Pronk D. 2001, MNRAS, 320, 401